RSC Sustainability

ROYAL SOCIETY OF CHEMISTRY

PAPER

View Article Online
View Journal

Cite this: DOI: 10.1039/d6su00231e

Dual-role iron catalyst for covalent triazine framework synthesis and efficient CO_2 cycloaddition under mild conditions

Mozhdeh Pourmansouri,[a] Negin Amiraslani,[a] Piero Mastrorilli,[b] Stefano Todisco[b] and Mojtaba Khorasani *[ac]

A pivotal yet often overlooked strategy in sustainable catalysis is the use of a single species for both catalyst synthesis and reaction mediation, thereby minimizing waste and resource consumption. Here, we demonstrate this integrative principle by employing an earth-abundant iron catalyst dually for constructing a covalent triazine framework (CTF) and for catalyzing CO_2 cycloaddition to epoxides under mild conditions. Direct condensation of melamine and dipicolinic acid, as commercially available precursors, in the presence of a catalytic amount of $FeCl_3$ under relatively mild conditions leads to the formation of an Fe-based catalyst (Fe-CTF-3) with remarkable surface area and pore volume of 683 $m^2\ g^{-1}$ and 1.34 $cm^3\ g^{-1}$, respectively. The role of the Fe catalyst, along with its loading and reaction time on CTF formation, was systematically investigated and discussed in the manuscript. It was found that the Fe centers control supersaturation, followed by nucleation and subsequent growth of the polymeric counterpart. All materials were characterized using various techniques to obtain accurate information about their physical, chemical, and textural properties. Fe-CTF-3 also displayed an exceptional turnover number (TON_c up to 3760) toward various types of epoxides under optimized conditions: 0.025 mol% catalyst, 0.125 mol% TBAB, 10 bar CO_2 at 70 °C within a short reaction time. To elucidate the distinct contributions of each catalytic component, a series of control experiments was performed under identical conditions. The catalyst was also recycled for 6 subsequent runs. In addition to the high catalytic activity of Fe-CTF-3 at an exceptionally low loading and its dual function in both catalyst synthesis and carbon dioxide conversion, it is noteworthy that reusable iron-catalyzed carbon dioxide coupling reactions have been rarely reported. The high catalytic performance of Fe-CTF-3 is attributed to the high surface area organic framework, which facilitates mass transfer and substrate diffusion, as well as the high nitrogen content that, in concert with uniformly dispersed Fe active sites, enhances CO_2 adsorption capacity. This study introduces a novel design strategy for multifunctional catalysts based on earth-abundant metals, enabling integrated pathways for material synthesis and application.

Received 21st April 2026
Accepted 5th June 2026

DOI: 10.1039/d6su00231e

rsc.li/rscsus

Sustainability spotlight

This work introduces a dual-role iron catalyst that both constructs a porous organic framework and subsequently catalyzes the conversion of CO_2 into cyclic carbonates under mild conditions. By using earth-abundant iron, commercially available precursors, and exceptionally low catalyst loadings (0.025 mol%), this strategy minimizes waste, energy input, and resource consumption. The catalyst is recyclable for six runs without loss of activity, and its high efficiency (TON_c up to 3760) reduces the need for hazardous co-catalysts or harsh reaction conditions. This integrative design principle where a single metal species directs both material synthesis and application, offers a sustainable blueprint for carbon capture and utilization technologies using non-precious metals.

Introduction

The uncontrolled release of carbon dioxide (CO_2) into the atmosphere, followed by global warming and climate change, represents one of the most pressing challenges of the current century and calls for the development of thoughtful and

[a]Department of Chemistry, Institute for Advanced Studies in Basic Sciences (IASBS), Zanjan 45137-66731, Iran. E-mail: m_khorasani@iasbs.ac.ir; Fax: +98-24-33153232; Tel: +98-24-33153223

[b]DICATECh Department, Politechnic of Bari, Via Orabona, 4 70125 Bari, Italy

[c]Research Center for Basic Sciences & Modern Technologies (RBST), Institute for Advanced Studies in Basic Sciences, IASBS, Zanjan 45137-66731, Iran

effective solutions. Although international agreements such as the Tokyo, Rio de Janeiro and Paris conventions have been established to address this issue, their global implementation remains inconsistent and lacks reliable enforcement.[1] In response, the European Union has introduced the Carbon Border Adjustment Mechanism (CBAM), a policy aimed at reducing global carbon emissions by applying carbon costs to imported goods, thereby harmonizing carbon pricing across borders and promoting cleaner production practices worldwide.[2] Consequently, the development of processes for capturing and converting carbon dioxide into high-value-added materials has gained increasing importance.[3,4] One notable transformation involves the coupling of carbon dioxide with epoxides to produce cyclic carbonates, which are widely used as polar aprotic solvents in fuel cells and organic synthesis, intermediates in pharmaceutical production, and precursors in polymer design.[5] This reaction may also serve as an efficient route for synthesizing *cis*-diols, with CO_2 acting as a temporary protecting group.[6] While this type of CO_2 transformation inherently aligns with the principles of green chemistry, growing attention is being directed toward the design of catalytic processes that rely on inexpensive and versatile precursors, operate under mild conditions, and require minimal amounts of catalyst and cocatalyst.[7]

Iron's affordability and minimal toxicity position it as a highly promising choice for developing innovative catalytic systems for CO_2 cycloaddition to epoxides.[8,9] To date, numerous homogeneous iron-based catalytic systems have demonstrated remarkable efficiency for this vital CO_2 transformation.[10–14] In homogeneous Fe-catalysis, the ligand architecture plays a pivotal role in modulating both the steric and electronic environment of the iron center, which in turn critically influences the observed catalytic activity.[8] Kleij and co-workers developed iron(III) complexes coordinated with aminotriphenol ligands, which demonstrated exceptional catalytic performance in the cycloaddition of CO_2 to terminal epoxides under mild reaction conditions.[6,15] Pescarmona and co-workers introduced iron pyridylamino-bis(phenolate) catalyst.[16] Kerton and co-workers introduced iron aminobis(phenolate) complexes.[17] Liu and co-workers reported the synthesis of iron pincer CNN and pyridine-based ONSN iron(III) complexes.[18,19] Kang and co-workers described the synthesis of an iron iminopyridine complex, which exhibited notable catalytic activity in relevant CO_2 conversion reactions.[20] Capacchione and co-workers introduced thioether-triphenolate bimetallic iron(III) complexes.[21,22] Döring and co-workers disclosed an ionic iron(-III) complex that operated as a single-component catalyst.[23] Despite their high catalytic activity, the limited reusability, pronounced moisture sensitivity, and reliance on costly ligand frameworks may hinder the broader applicability of these systems. While post-synthetic modification of diverse porous supports using homogeneous analogues of iron-based catalysts has partially mitigated some of the above challenges, the persistent issues of non-uniform catalyst distribution and channel blockage continue to impose significant limitations on catalytic performance.[24] Accordingly, catalyst design strategies have turned to embed the metal directly within porous architectures such as metal–organic frameworks (MOFs).[25–29] Another strategy involves embedding iron catalyst species within the organic porous matrix in a manner that simultaneously preserves a high contact surface area and ensures accessibility to the catalytically active sites, an approach that has been seldom investigated. For example, Cho *et al.* developed a new series of hollow microporous disalphen networks designed for the preparation of iron-based catalysts for CO_2 fixation into cyclic carbonates.[30] Also, in 2023, Nagaraja and co-workers developed an iron(III)-porphyrin-based ionic porous organic polymer incorporating nucleophilic bromide functionalities, which enabled the direct one-pot transformation of olefins and CO_2 into cyclic carbonates.[31] However, a conceptually distinct approach in which the metal catalyst used to construct a porous organic framework remains embedded as the active site for subsequent transformations remains largely unexplored, particularly for earth-abundant metals like iron.

Covalent Triazine Frameworks (CTFs) are a distinctive class of porous organic polymers characterized by their triazine units and high nitrogen content, which impart remarkable thermal and chemical stabilities.[32,33] Recent progress in metal-functionalized CTFs has expanded their use in CO_2 conversion, as the abundant nitrogen sites offer a dual function for capturing CO_2 molecules and coordinating with metal centers to create active catalytic sites.[34,35] The CTF synthesis method is expected to enable the controlled incorporation of various functional groups and metal atoms into the framework.[36] Since the first report on CTF synthesis, where $ZnCl_2$ was used as both reaction medium and catalyst, a wide range of nitrile-containing monomers has been introduced for the construction of triazine-based organic frameworks.[37–39] Although these CTFs are synthesized *via* the cyclotrimerization of aromatic nitriles, providing tunable porosity, extended π-conjugation, and versatile coordination environments, their synthesis is inherently constrained by the requirement for high temperatures, harsh reaction conditions, and the occurrence of undesired side reactions.[40] In this regard, metal-catalyzed intermolecular reactions involving triazine-containing precursors can also lead to the formation of CTF structures under milder reaction conditions. For instance, several metal-catalyzed reactions have been employed to synthesize new CTF structures, including Friedel–Crafts alkylation (using Al-based catalysts), Sonogashira coupling (Pd and Cu catalysts), Yamamoto coupling (Ni catalyst), Suzuki–Miyaura coupling (Pd catalyst), and Stille cross-coupling (Pd catalyst).[41–45] Recently, Das *et al.* reported that $Cu(OTf)_2$ can serve as an effective catalyst for the synthesis of a new series of covalent organic frameworks containing triazine rings through a multicomponent reaction strategy.[46] A noteworthy aspect of the previously reported CTFs is that the expensive metal catalyst employed during synthesis must be finally removed to avoid interference with the practical processes under investigation. To the best of our knowledge, the concept of utilizing the same metal, originally introduced during CTF preparation, as a catalytically active site in subsequent transformations has been rarely explored. Based on the above considerations, it would be highly valuable to design new CTF structures using commercially

available precursors and their intermolecular reactions under mild reaction conditions, facilitated by low-cost metal catalysts that not only drive the CTF formation but also serve as active sites for subsequent chemical transformations. We previously demonstrated that supported dipicolinic acid (DPA) derivatives can serve as effective solid ligands for coordinating nickel and lanthanum catalysts, thereby enabling the direct coupling of CO_2 with epoxides.[47,48] Building on this foundation, and motivated by the superior sustainability profile of iron, we now report the development of an iron-based covalent triazine framework (Fe-CTF) constructed from DPA and melamine. This catalyst promotes the same transformation under mild conditions, achieving an excellent turnover number of up to 3920 while requiring only a minimal co-catalyst loading (0.125 mol%). In this work, we (i) demonstrate $FeCl_3$ as a dual-function catalyst for CTF synthesis and CO_2 fixation, (ii) elucidate the role of Fe in controlling framework porosity, (iii) achieve exceptional activity at ultralow loadings, and (iv) provide mechanistic insights into the synergistic catalysis.

Experimental

Synthesis of Fe-CTF-3

Melamine (0.427 g, 3.3 mmol) was dissolved in 10 mL of DMSO. Then, dipicolinic acid (0.835 g, 5 mmol) and anhydrous $FeCl_3$ (0.051 g, 3 mol%) were added to the solution. The mixture was heated at 140 °C for 48 hours. After cooling to room temperature, the resulting precipitate was collected by filtration. The solid was washed sequentially with DMSO, deionized water, and ethanol, followed by soaking in acetone for 24 hours. The final Fe-CTF-3 material was dried at 100 °C (0.79 g, 73%).

CTF-1 was prepared using the same procedure but without the $FeCl_3$ catalyst (0.379 g, 35%). For the synthesis of Fe-CTF-2, 0.102 g (6 mol%) of $FeCl_3$ catalyst was used (0.595 g, 55%). Fe-CTF-4 was obtained within 24 h (0.476 g, 44%).

CO_2 cycloaddition to epoxide catalyzed by Fe-CTF-3

A stainless-steel high-pressure reactor was loaded with epoxide (10 mmol), Fe-CTF-3 catalyst (0.050 g, 0.025 mol%), and tetrabutylammonium bromide (TBAB) (0.004 g, 0.125 mol%). The system was gradually pressurized to 10 bar CO_2 and stirred continuously at 70 °C for the specified reaction time. After completion, the reactor was cooled to room temperature and slowly depressurized to ensure safety and prevent sample loss. To aid in catalyst separation, 5 mL of ethyl acetate was added to the reaction mixture. The supernatant was then carefully decanted and analyzed by gas chromatography using trimethylbenzene (TMB) as an internal standard. The product was purified by column chromatography with an ethyl acetate/*n*-hexane solvent mixture (1 : 5, v/v), and its structure was confirmed by ^{1}H-NMR spectroscopy.

Reusability studies of Fe-CTF-3 in the CO_2 cycloaddition to styrene oxide

After the first catalytic cycle, the Fe-CTF-3 catalyst was recovered, thoroughly washed with dichloromethane (2 × 10 mL) and hot ethanol (2 × 10 mL), dried under vacuum overnight, and then reused under the same reaction conditions in subsequent runs. For each reuse cycle, a stainless-steel high-pressure reactor was charged with styrene oxide (10 mmol), the recovered Fe-CTF-3 catalyst, and TBAB (0.004 g, 0.125 mol%). The system was gradually pressurized to 10 bar of CO_2 and stirred continuously at 70 °C for 10 h. The work-up, conversion calculations, catalyst washing, drying, and recycling steps were then repeated accordingly.

Results and discussion

During the synthesis of CTF from dipicolinic acid and melamine, we observed several interesting phenomena (Scheme 1). It was found that the solvent volume primarily influences whether CTF formation occurs, while the catalytic loading of $FeCl_3$ determines whether the resulting framework exhibits a high or low surface area. The CTF formation did not occur in a transparent solution of monomers in 30 mL of DMSO at 140 °C (Table S1, entry 1). Interestingly, decreasing the solvent volume to 10 mL facilitated the formation of a solid polymeric network denoted as CTF-1 (Table S1, entry 2). CTF-1 exhibited a Type II isotherm according to IUPAC classification (Fig. 1a).[49] The Brunauer–Emmett–Teller surface area (S_{BET}) and total pore volume (V_t) for this sample were 100 $m^2\ g^{-1}$ and 0.75 $cm^3\ g^{-1}$, respectively (Table S1, entry 2). In the presence of 6 mol% $FeCl_3$, a new polymeric material denoted as Fe-CTF-2 was obtained in a moderate yield of 55% from a totally transparent solution of monomers and catalyst (Table S1, entry 3). Similar to the previously synthesized material, Fe-CTF-2 showed a Type II nitrogen adsorption isotherm, with a pronounced nitrogen uptake observed at a relative pressure of 0.95 (Fig. 2b). The S_{BET}

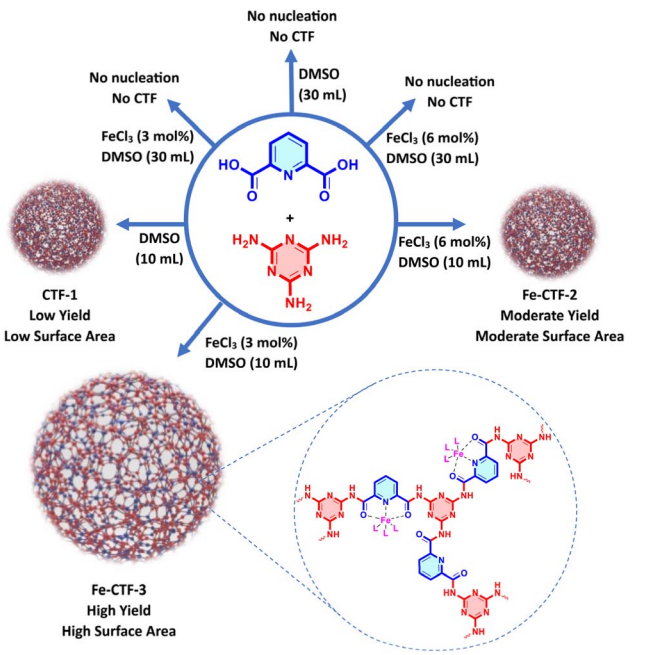

Scheme 1 Effect of solvent volume and catalyst loading on textural properties of CTF derived from dipicolinic acid and melamine.

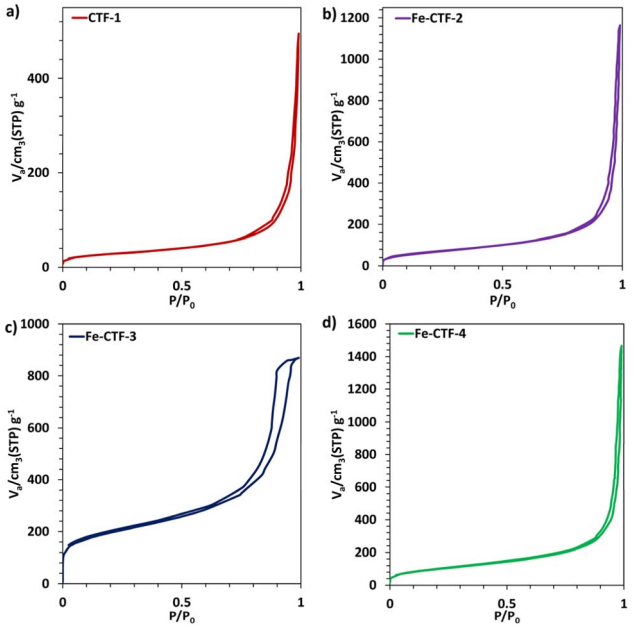

Fig. 1 The nitrogen adsorption–desorption isotherms for (a) CTF-1, (b) Fe-CTF-2, (c) Fe-CTF-3, and (d) Fe-CTF-4.

and V_t of Fe-CTF-2 were found to be 245 m^2 g^{-1} and 1.80 cm^3 g^{-1}, respectively (Table S1, entry 3). Interestingly, reducing the $FeCl_3$ catalyst loading to 3 mol% resulted in the formation of Fe-CTF-3 in good yield of 73%, which exhibited a significantly enhanced S_{BET} of 683 m^2 g^{-1} and a V_t of 1.34 cm^3 g^{-1} (Table S1, entry 4). Fe-CTF-3 displayed a Type IV nitrogen adsorption isotherm with a characteristic H1 hysteresis loop, which is typically associated with the presence of mesopores channels (Fig. 1c). Reducing the reaction time to 24 hours led to the formation of Fe-CTF-4, obtained in a moderate yield of 44% (Table S1, entry 5). A Type II isotherm was also observed for the Fe-CTF-4 sample (Fig. 1d). The S_{BET} and total V_t of this sample were 348 m^2 g^{-1} and 2.26 cm^3 g^{-1}, respectively (Table S1, entry 5). It is worth noting that, despite the moderate to high surface areas of the synthesized catalysts, Barrett–Joyner–Halenda pore size analysis (D_{BJH}) revealed a lack of well-defined pore size distributions across all samples (Fig. S1–4). This absence of pore regularity may be attributed to the non-directional nature of polymer growth, which does not proceed along a distinct planar axis, thereby preventing the formation of layered porous architectures. Returning to the main discussion, the formation of CTF in this irreversible polycondensation system is governed by classic nucleation theory, where the critical parameters are the effective monomer concentration and the rate of oligomer generation.[50,51] At 140 °C, dipicolinic acid and melamine dissolve in DMSO and undergo condensation to form initial oligomers in the solution. At high DMSO volumes (30 mL), the low concentration prevents the reaction polymerization from reaching the solubility product of the oligomeric nuclei, so nucleation does not occur. Reducing the volume to 10 mL increases the concentration, shifting the equilibrium and allowing supersaturation to be achieved. During this process, soluble monomers are continuously integrated into the developing CTF framework. $FeCl_3$ catalyzes the polymerization steps and facilitates oligomer formation, resulting in a rapid progression toward supersaturation and nucleation. A high catalyst loading (6 mol%) drives rapid oligomerization, leading to a burst of nucleation and the growth of a dense, kinetically trapped polymer (Fe-CTF-2) with moderate surface area. In contrast, using 3 mol% $FeCl_3$ appears to place the system between two above boundary conditions; the reaction rate becomes more controlled, and supersaturation is reliably achieved. In fact, a lower catalyst loading (3 mol%) adjusts the condensation rate, allowing the system to approach a more controlled nucleation and growth regime. This facilitates the development of a more extended and porous network (Fe-CTF-3), as evidenced by its Type IV isotherm and significantly higher surface area. The correspondingly high pore volumes observed for Fe-CTF-2 and Fe-CTF-4 (>1.8 cm^3 g^{-1}) suggest the formation of macroporous or loosely packed morphologies. Notably, the irreversible nature of the amide linkage precludes the structural reorganization necessary for long-range pore ordering. Consequently, all materials exhibit broad pore size distributions. These observations highlight that in irreversible framework syntheses, porosity is not a default outcome but a carefully tunable property achieved by balancing concentration-driven thermodynamics with catalyst-controlled kinetics. Particularly, no CTF formation was observed at high solvent volumes, regardless of whether 3 or 6 mol% of $FeCl_3$ was used (Table S1, entries 6 and 7). This suggests that at low reactant concentrations, even the presence of a catalyst is insufficient to achieve the supersaturation necessary for nucleation. Additionally, we investigated the possibility of forming a metal–organic framework between $FeCl_3$ and DPA in the absence of melamine (Table S1, entry 8). The results clearly

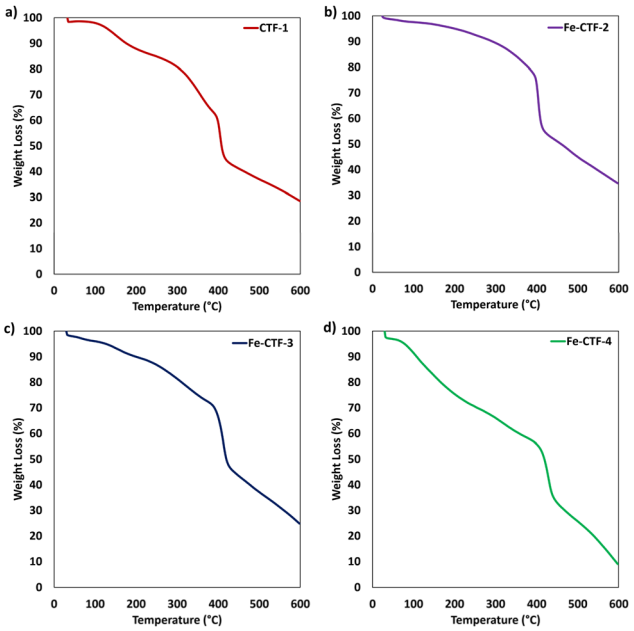

Fig. 2 The TG patterns for (a) CTF-1, (b) Fe-CTF-2, (c) Fe-CTF-3, and (d) Fe-CTF-4.

rule out any MOF formation under the specified conditions, no solid material was observed.

The thermal stability of the synthesized CTFs was systematically evaluated. The thermogravimetric analysis (TGA) results offer valuable insights into the degree of polymerization across different samples (Fig. 2a–d). All CTF samples exhibited minimal weight loss below 100 °C, which is attributed to the evaporation of physically adsorbed volatile solvents. The primary decomposition of the CTF backbone occurred between 350 °C and 450 °C, indicating the thermal degradation of the polymer network. Interestingly, samples such as CTF-1 and Fe-CTF-4, which were expected to have an incomplete degree of polymerization due to either the absence of a catalyst or insufficient reaction time, showed a noticeable weight loss below 300 °C (Fig. 2a and d). This early degradation is likely due to the breakdown of edge-located DPA and melamine units that were not fully integrated into the polymer matrix. In contrast, Fe-CTF-3 and Fe-CTF-4, synthesized with the aid of an iron-based catalyst, demonstrated a sharp and well-defined weight loss in the range of 390–450 °C (Fig. 2b and c), consistent with a more complete and thermally stable polymerization process. These results indicate a more uniform and complete polymerization and further highlight the crucial role of the Fe catalyst in facilitating the formation of a stable CTF network. Inductively coupled plasma optical emission spectroscopy (ICP-OES) revealed that the Fe contents of Fe-CTF-2, Fe-CTF-3, and Fe-CTF-4 were 0.11, 0.05, and 0.03 mmol g^{-1}, respectively.

The presence of functional groups and characteristic bonds in the synthesized CTFs was further elucidated by Fourier transform infrared (FTIR) spectroscopy (Fig. 3a). For comparative analysis, spectra of the DPA and melamine were also included. The disappearance of the characteristic peaks corresponding to amine (~3300 cm^{-1}) and carboxylic acid (~1700 cm^{-1}) groups in monomers confirms their successful polymerization. The sharp absorption band at ~1550 cm^{-1} is attributed to the stretching vibration of C=N bonds in triazine rings, while the peaks around ~1500 cm^{-1} are assigned to C=C stretching in the aromatic rings of DPA precursors. Additionally, the emergence of a new band near ~1650 cm^{-1} indicates the formation of amide linkages. The cross-polarization/magic angle spinning ^{13}C nuclear magnetic resonance (CP-MAS ^{13}C-NMR) spectrum of the CTFs exhibited significant broadening of all resonances (Fig. 3b, S5, and S6). The intense, relatively sharp peak at δ 166.4 ppm is attributable to the equivalent carbons of the triazine ring of melamine. The broad signals at approximately δ 55 ppm and approximately δ 13 ppm are tentatively attributed to the three C-H carbons of the pyridine ring and the quaternary C of the pyridine ring, respectively, with the latter being overlapped by the amidic C=O bond of the dipicolinic moiety. These attributions were made on the assumption that the carbons of the dipicolinic units undergo an isotropic shift towards high fields (induced by the paramagnetism of Fe(III) in a low-spin state of $S = 1/2$) that is greater than that experienced by the carbons of the triazine rings. Powder X-ray diffraction (PXRD) patterns in the low-angle region (2θ = 0–4.5°) are typically used to identify structural features associated with the porous architecture of CTFs. In this case, the absence of distinct peaks in all samples suggests a lack of long-range pore architecture within the CTF network, which aligns well with the BJH pore size distribution results (Fig. 3c). Also, the wide-angle PXRD patterns (2θ = 5–80°) are broad and featureless, indicative of the amorphous or poorly crystalline

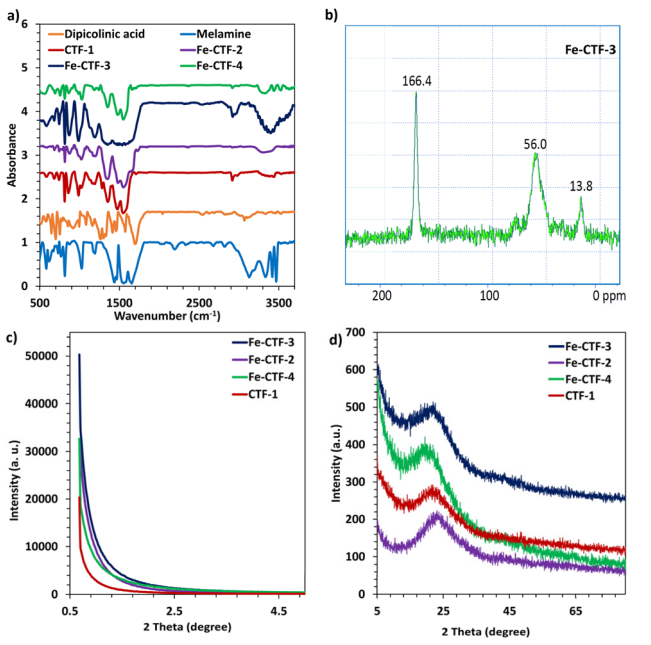

Fig. 3 (a) FTIR spectra for all synthesized CTFs. (b) CP-MAS ^{13}C-NMR for Fe-CTF-3. (c) Low angle and (d) wide angle XRD patterns for CTFs.

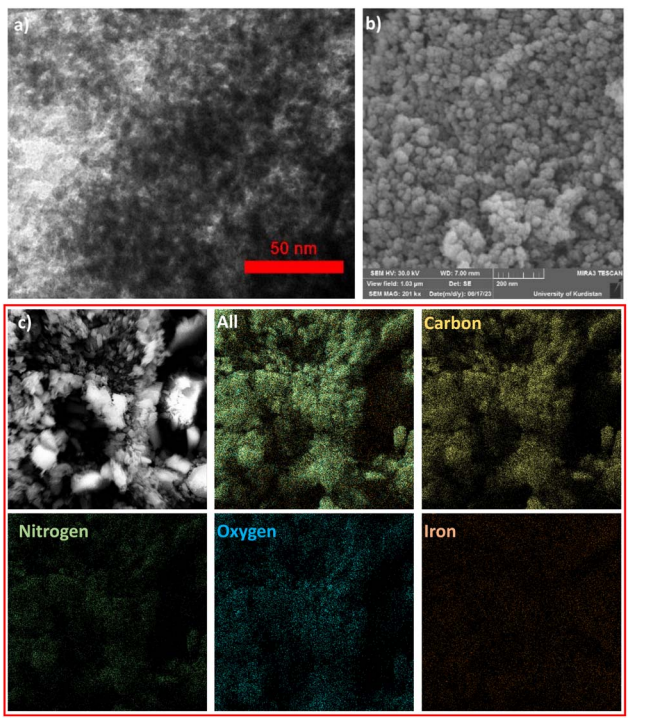

Fig. 4 (a) TEM image (b) SEM image and (c) EDS-elemental mapping for Fe-CTF-3.

nature of the materials (Fig. 3d). Fe-CTF-3 exhibited a notably high CO_2 adsorption capacity of 2.65 mmol g^{-1} at 1 bar and room temperature (Fig. S7). This enhanced uptake can be attributed to the synergistic presence of dipicolinic amide functionalities and electron-rich triazine moieties within the porous CTF framework, which collectively promote strong interactions with CO_2 molecules.

The transmission electron microscopy (TEM) image indicated formation of a porous network but without observable pore ordering in Fe-CTF-3 (Fig. 4a). The scanning electron microscopy (SEM) revealed a spherical morphology with relatively agglomerated particles for Fe-CTF-3 (Fig. 4b). The presence of expected elements was further confirmed by elemental mapping by energy dispersive spectroscopy (EDS) coupled with SEM. As it is clear, all expected elements such as nitrogen, carbon, oxygen, and iron are uniformly distributed to the Fe-CTF-3 catalyst (Fig. 4c). The integrity and oxidation state of this element were also investigated by X-ray photoelectron spectroscopy (XPS) technique (Fig. 5). The XPS survey of Fe-CTF-3 confirmed the presence of all expected elements (Fig. 5a). The C 1 s spectrum was deconvoluted into three peaks located at approximately 284, 286, and 287 eV (Fig. 5b). The peak at ~284 eV corresponds to C=C and C–C bonds, while the peak at ~286 eV is attributed to C=N bonds present in both triazine and pyridine units. The peak at ~287 eV is associated with carbonyl functionalities originating from the DPA linkers. The N 1s spectrum was resolved into two distinct peaks (Fig. 5c): the lower binding energy peak at 397.5 eV is assigned to nitrogen atoms in triazine rings, whereas the higher energy peak at 399 eV corresponds to electron-deficient nitrogen atoms in the amide moieties. Iron species were identified by two well-defined peaks at 709 eV and 722.2 eV, with a spin–orbit splitting of 13.2 eV, consistent with Fe(III) $2p_{3/2}$ and Fe(III) $2p_{1/2}$, respectively (Fig. 5d).

We then shifted our focus to the direct coupling of CO_2 with styrene oxide as the substrate model, aiming to identify optimal reaction conditions by systematically evaluating parameters such as catalyst loading, co-catalyst type and loading, CO_2 pressure, reaction time, and temperature. All reaction yields were determined by gas chromatography using TMB as the internal standard. To accurately assess the role of Fe-CTF catalysts, the yield of the co-catalyst alone must be subtracted from the overall yield of the binary metal/co-catalyst system, as is well documented.[47,52,53] Therefore, we have used the corrected turnover number (TON_c) herein, which accounts for the contribution of each co-catalyst to the total TON. Fe-CTF-3 was selected as the main catalyst due to its excellent porosity and textural properties. Throughout the optimization studies, we consistently employed very low catalyst loadings, as preliminary experiments revealed the high intrinsic activity of the Fe-CTF-3 catalyst. We first investigated the effect of tetrabutylammonium bromide (TBAB) loading, which emerges as the most effective co-catalyst (Table 1, entries 1–4). Remarkably, a low catalyst loading of 0.025 mol% Fe-CTF-3 under 10 bar CO_2 at 70 °C for 10 hours yielded promising results when 0.125 mol% of TBAB was employed as the co-catalyst (Table 1, entry 4). However, reducing TBAB loading to 0.062 mol% led to a sharp decline in yield of styrene carbonate (42%), indicating a threshold concentration necessary for efficient catalysis (Table 1, entry 5). It was observed that while the catalyst maintained its activity and selectivity at an elevated temperature of 80 °C, the reaction yield of styrene carbonate significantly dropped to 40% at 60 °C (Table 1, entries 6 and 7). A slight decrease from 0.025 mol% to 0.01 mol% of Fe-CTF-3 led to a reduction in reaction yield, emphasizing the importance of sufficient active site availability for high turnover (Table 1, entry 8). Despite achieving full conversion at 10 bar CO_2 pressure, reducing the pressure to 7.5 and 5 bar resulted in significantly lower yields of 66% and 22%, respectively (Table 1, entries 9 and 10). This trend highlights the critical role of CO_2 concentration in driving the equilibrium toward cyclic carbonate formation. Our studies demonstrated that a prolonged exposure of 10 hours is crucial for achieving complete conversion. Reducing the reaction time to 7, 5, and 2 hours resulted in yields of 80%, 50%, and 23%, respectively (Table 1, entries 11–13). The nature of the co-catalyst and its interaction with the active metal centers plays a pivotal role in the cycloaddition of CO_2 to epoxides.[54] In this regard, we evaluated the performance of Fe-CTF-3 as a heterogeneous catalyst in combination with various co-catalysts under solvent-free conditions. Tetrabutylammonium iodide (TBAI) showed moderate activity of 54%, which was lower than expected given the higher nucleophilicity of iodide ions (Table 1, entry 14). Tetrabutylammonium chloride (TBAC), tetraethylammonium bromide (TEAB) and 1,4-diazabicyclo[2.2.2]octane (DABCO) were ineffective (Table 1, entries 15–17). Tetrabutylammonium tetrafluoroborate ($TBABF_4$), a non-nucleophilic co-catalyst, resulted in negligible conversion, reinforcing the necessity of a nucleophilic halide for epoxide activation step (Table 1, entry 18). Although iodide is generally more nucleophilic, the higher activity of TBAB over TBAI in our system is explained by specific factors. The larger ionic radius of iodide ions likely hinders their diffusion into the mesopores of Fe-CTF-3, and stronger Fe–I interactions may poison the iron centers. Regarding the other co-catalysts, their poor activity stems from either lower

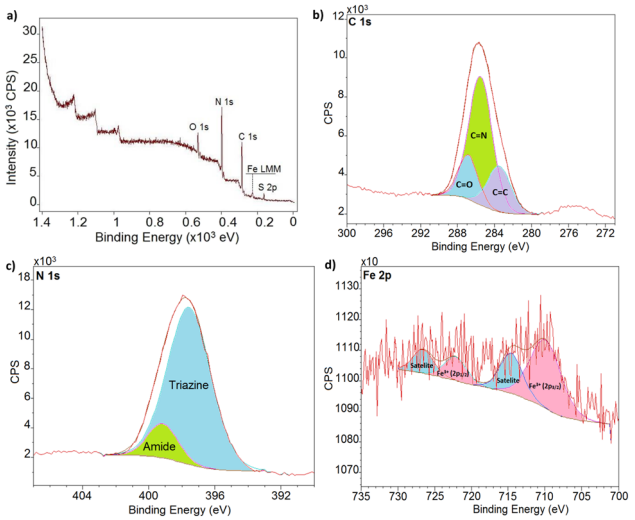

Fig. 5 XPX spectrum of Fe-CTF-3 (a) survey, (b) C 1s, (c) N 1s, (d) Fe 2p.

Table 1 The possible coupling of CO_2 with styrene oxide catalyzed by the prepared catalyst under various reaction conditions[a]

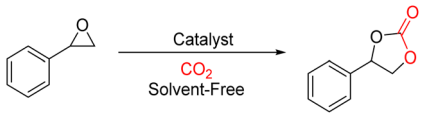

Entry	Catalyst	co-Cat. (mol%)	P_{CO_2} (bar)	Time (h)	Yield[b] (%)	TON_c[c]
1	Fe-CTF-3	TBAB (1)	10	10	98 (62)	1440
2	Fe-CTF-3	TBAB (0.5)	10	10	98 (26)	2880
3	Fe-CTF-3	TBAB (0.25)	10	10	98 (22)	3040
4	**Fe-CTF-3**	**TBAB (0.125)**	**10**	**10**	**98** (21)	3080
5	Fe-CTF-3	TBAB (0.062)	10	10	42 (6)	1440
6[d]	Fe-CTF-3	TBAB (0.125)	10	10	98 (38)	2400
7[e]	Fe-CTF-3	TBAB (0.125)	10	10	40 (8)	1280
8[f]	Fe-CTF-3	TBAB (0.125)	10	10	72 (21)	2040
9	Fe-CTF-3	TBAB (0.125)	7.5	10	66 (9)	2280
10	Fe-CTF-3	TBAB (0.125)	5	10	22 (9)	520
11	Fe-CTF-3	TBAB (0.125)	10	7	80 (18)	2480
12	Fe-CTF-3	TBAB (0.125)	10	5	50 (7)	1720
13	Fe-CTF-3	TBAB (0.125)	10	2	23 (4)	760
14	Fe-CTF-3	TBAI (0.125)	10	10	54 (25)	1160
15	Fe-CTF-3	TBAC (0.125)	10	10	10 (9)	40
16	Fe-CTF-3	TEAB (0.125)	10	10	9 (4)	200
17	Fe-CTF-3	DABCO (0.125)	10	10	5 (1)	160
18	Fe-CTF-3	$TBABF_4$ (0.125)	10	10	>2 (—)	—
19	Fe-CTF-3	—	10	10	>2 (—)	—
20	—	TBAB (0.125)	10	10	21	—
21	CTF-1	TBAB (0.125)	10	10	53 (21)	—
22	Monomer	TBAB (0.125)	10	10	30 (21)	—
23	Melamine + DPA	TBAB (0.125)	10	10	>2 (—)	—
24	Fe-CTF-2	TBAB (0.125)	10	10	30 (21)	360
25	Fe-CTF-4	TBAB (0.125)	10	10	40 (21)	760

[a] Reaction conditions: styrene oxide (10 mmol), Fe-CTF-3 (50 mg, 0.025 mol%) at 70 °C unless otherwise stated. [b] GC yield by using TMB as internal standard. The number in parentheses indicates the reaction yield in the presence of the co-catalyst alone. [c] The corrected turnover numbers were determined by [(yield of styrene carbonate with Fe-based catalyst + co-catalyst) − (yield of styrene carbonate with co-catalyst alone)/Fe mol%]. [d] At 80 °C. [e] At 60 °C. [f] 40 mg, 0.020 mol% Fe-CTF-3.

nucleophilicity (TBAC), lower solubility (TEAB), weak epoxide ring-opening ability (DABCO), or the lack of a nucleophilic halide ($TBABF_4$).[53] Therefore, the optimized reaction conditions were identified as 10 mmol styrene oxide, 0.025 mol% Fe-CTF-3, 0.125 mol% TBAB, and 10 bar CO_2 at 70 °C for 10 hours (Table 1, Entry 4). Under these conditions, the TON_c approaches 3080, highlighting the outstanding efficiency of the presented catalytic systems. The outstanding catalytic efficiency of Fe-CTF-3 under notably mild conditions (0.025 mol% catalyst, 10 bar CO_2, 70 °C) arises from a synergistic interplay of three key structural attributes. First, its high surface area and mesoporous architecture (683 $m^2\ g^{-1}$) maximize the accessibility of active sites and enable rapid diffusion of reactants. Second, the Fe-CTF framework exhibits intrinsic bifunctionality: Fe(III) centers act as strong Lewis acids to activate epoxides, while the triazine units enhance CO_2 capture and polarization in the local environment. Together, these features establish a highly effective nanoreactor in which reactants are concentrated, pre-activated, and transformed with minimal diffusion constraints. Additionally, the synergistic interaction between the Fe centers and the TBAB likely enhances the activation of styrene oxide and promotes efficient CO_2 insertion. Control experiments further elucidated the roles of individual components. Fe-CTF-3 alone was inactive, while TBAB alone yielded only 21% under identical conditions (Table 1, Entries 19 and 20). The combination of CTF-1 and TBAB achieved a moderate yield of 53%, suggesting that the presence of Fe centers, even at ppm levels, is essential for full catalytic activity (Table 1, Entry 21). It was found that monomer analogous (see experimental section for details) just resulted in 30% styrene carbonate (Table 1, entry 22). Therefore, the porous framework functions as a nanoreactor, not only adsorbing and concentrating CO_2 in proximity to the Fe catalytic sites, but also facilitating efficient substrate diffusion. Especially, mixed systems such as melamine + DPA failed to deliver significant yields, likely due to the lack of a porous structure to trap carbon dioxide molecules (Table 1, Entry 25). The above studies clearly demonstrate that each component of the catalytic system plays an essential role in achieving optimal results. To confirm that neither polyester nor polycarbonate was generated during the catalytic reaction, the crude mixture was subjected directly to ^{1}H-NMR analysis. The resulting spectrum displayed no signals attributable to

polymeric species, thereby verifying that polymerization had not occurred (Figure S8). Importantly, even under CO_2-free conditions, no evidence of polyether formation was observed (Fig. S8). These observations prove the high selectivity of the Fe-CTF-3. Interestingly, under optimized reaction conditions, Fe-CTF-2 and Fe-CTF-4 displayed poor results of 30 and 40%, respectively. These results indicate that iron alone does not achieve such high yields; rather, its incorporation into a porous organic network, combined with a high surface area and an appropriate distribution of functional groups, appears to be essential.

To evaluate the versatility of the developed catalytic method, a range of epoxides was subjected to check under the optimized reaction conditions. Epichlorohydrin could be selectively transformed to the corresponding epichlorohydrin carbonate in excellent yield of 98% within short reaction time (Table 2, entry 1). Propylene oxide underwent efficient transformation into propylene carbonate which is a widely used polar aprotic solvent with an outstanding yield of 98% (Table 2, entry 2).

Table 2 Substrate scope for the synthesis of 5-ring cyclic carbonates catalyzed by Fe-CTF-3[a]

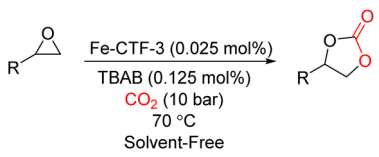

Entry	Epoxide	t (h)	GC yield[b] (%)	TON_c[c]	TOF_c[d]
1		5	98 (42)	2240	448
2		5	98 (4)	3760	752
3		5	91 (4)	3480	696
4	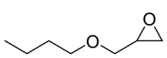	5	96 (21)	3000	600
5	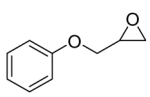	10	93 (27)	2640	264
6	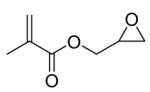	10	98 (9)	3560	356
7	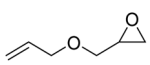	10	94 (8)	3440	344
8		24 24[e]	37 (6) 50 (16)	1240 1360	52 57

[a] Reaction conditions: epoxide (10 mmol), Fe-CTF-3 (50 mg, 0.025 mol%), TBAB (4 mg, 0.125 mol%) and CO_2 pressure (10 bar) at 70 °C. [b] All carbonate yields were determined by the GC technique with TMB as an internal standard. The number in parentheses indicates the reaction yield in the presence of the co-catalyst alone. [c] TON_c = [(carbonate yield with Fe-CTF-3 + TBAB) − (carbonate yield with TBAB alone)]/(mol% Fe). [d] TOF_c = TON_c/time. [e] 0.5 mol% TBAB.

Similarly, butylene oxide was converted with high selectivity into 1,2-butylene carbonate, also in excellent yield (Table 2, entry 3). When *n*-butyl glycidyl ether, featuring a longer alkyl chain, was employed, the corresponding cyclic carbonate was obtained with excellent selectivity and yield (Table 2, entry 4). It is worth mentioning that the yield, which is not slightly reduced compared to that of smaller epoxides, highlights the higher activity and potential of the catalytic protocol presented. Phenyl glycidyl ether also reacted smoothly with CO_2, affording the desired five-membered cyclic carbonate in 93% yield (Table 2, entry 5). Impressively, substrates containing sensitive carbon–carbon double bonds such as methyl meta-acrylate glycidyl ether and allyl glycidyl ether, were converted into their respective cyclic carbonates without any concern of polymerization or side reactions (Table 2, entries 6 and 7). Even cyclohexene oxide, typically considered less reactive in CO_2 cycloaddition, was converted into the corresponding cyclic carbonate with a moderate yield of 50% after 24 hours, without any indication of polymerization (Table 2, entry 8). These findings collectively demonstrate that the Fe-CTF-3 catalyst, offers a robust and selective platform for the synthesis of five-membered cyclic carbonates from terminal epoxides under mild conditions and excellent TONs.

We propose a mechanistic pathway for the Fe-CTF-3 catalyzed conversion of CO_2 and epoxides into cyclic carbonates, emphasizing the complementary functions of the framework's chemical motifs and the associated metal/co-catalyst ensemble (Fig. 6). Our observations during the reference catalyst studies, namely (i) the activity difference between Fe-CTF-3 and CTF-1, (ii) the activity difference between CTF-1 and TBAB alone, as well as literature precedent for triazine-mediated CO_2 activation, collectively support the following proposed mechanistic cycle. The catalytic cycle begins with dual substrate activation at distinct sites: (i) CO_2 is physisorbed and polarized by the triazine groups of the CTF,[55] while (ii) the epoxide is coordinated and electrophilically activated at the Lewis acidic Fe(III)

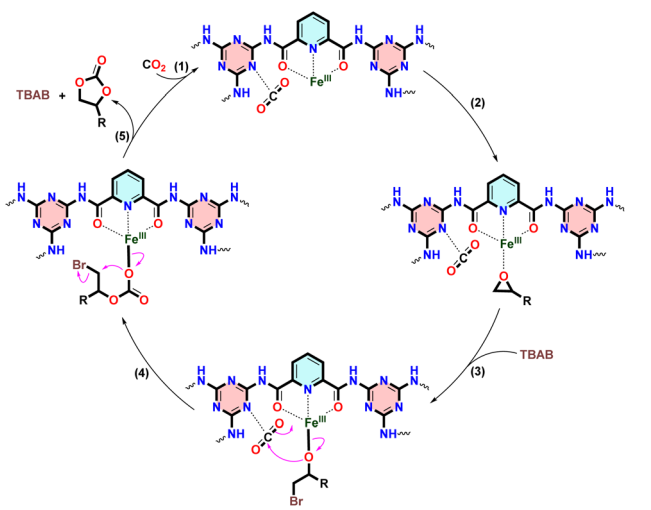

Fig. 6 Proposed reaction mechanism for the coupling of CO_2 with epoxides catalyzed by Fe-CTF-3. For clarity, the ligands surrounding Fe(III) were not shown.

Table 3 Comparison of Fe-CTF-3 with other heterogeneous Fe-based catalysts toward CO_2 cycloaddition to SO

Entry	Catalyst	TBAB (mol%)	CO_2 (bar)	T (C)	t (h)	Yield (%)	TON	Ref.
1	NH_2-MIL-101	12.5	1	rt	5	55	12	25
2	NH_2-MIL-101	12.5	1	rt	2.5	99 (PO)	22	25
3[a]	Fe-Zr-MOF-5	3	10	120	12	96 (PO)	204	26
4	$FeCO_2$-MOF	5	1	80	8	99	248	27
5[b]	DAP-Fe-MOF	10	1	65	1	95	135	28
6[c]	MOF-919-Cu-Fe	107	1	rt	24	99	NR	29
7[c]	MOF-919-Cu-Fe	107	1	rt	24	99 (PO)	NR	29
8[d]	H-MFeSN	0.2	20	100	9	97 (PO)	1950	30
9	H-MFeSN	0.2	20	100	9	78	1568	30
10[e]	FePC@MWCNTs	—	25	125	24	58	11 100	56
11	Fe-CTF-3	0.125	5	70	10	98 (PO)	3920	This work
12	Fe-CTF-3	0.125	10	70	10	98	3920	This work

[a] In DMF. [b] MIL-88-NH_2(Fe) conjugated dialdehyde pectin. [c] In MeCN. [d] Iron(III) ions incorporated into the hollow and microporous disalphen networks. [e] Iron phthalocyanine/imidazolium bromide co-polymer covalently attached to the surface of multi-walled carbon nanotubes.

center (Steps 1 and 2). This cooperative activation strategy is essential for reducing the energetic barriers of the subsequent transformations. In Step 3, the bromide anion supplied by TBAB attacks the β-carbon of the Fe-bound epoxide in a regioselective, kinetically controlled manner, producing a Fe-associated alkoxide intermediate. Step 4 involves the insertion of the pre-activated CO_2 into the Fe-O bond, generating a metallocarbonate species. Finally, Step 5 proceeds *via* intramolecular nucleophilic displacement, closing the ring to form the cyclic carbonate product and regenerating both catalyst and co-catalyst for the next cycle. This mechanistic framework underscores a clear division of labor, the CTF scaffold concentrates and activates CO_2, while the Fe-TBAB pair governs epoxide activation and directs the sequence of bond-forming steps. The reusability of Fe-CTF-3 was assessed under optimized conditions. Following each run, the catalyst was recovered by simple centrifugation, washed with ethanol and dichloromethane, and dried prior to reuse. Across six consecutive cycles, no loss of activity or selectivity was detected (Fig. S9), confirming excellent operational stability. In the seventh run, however, the yield decreased to 83%. Characterization of the recycled Fe-CTF-3 verified its structural robustness. Nitrogen physisorption revealed an identical isotherm and a surface area of 308 $m^2\ g^{-1}$ with a pore volume of 0.6 $m^3\ g^{-1}$ (Fig. S10). The slight reduction in surface area compared to the fresh catalyst is attributed to the retention of styrene carbonate products within the organic framework of catalyst, which may partially hinder catalytic activity. Thermogravimetric analysis further demonstrated that the recycled catalyst undergoes a similar three-step degradation between 100 and 600 °C as the pristine material (Fig. S12). Notably, the weight loss below 350 °C was significantly greater for the recycled sample, consistent with the presence of cyclic carbonate products trapped within the structure. The FTIR results for the recovered catalyst were in good agreement with previous analyses (Fig. S13). The broad peak around 1650 cm^{-1} clearly confirms the presence of residual cyclic carbonate in the organic backbone of the catalyst. It is clear that all expected peaks are still observed, indicating that the structure of the catalyst remained intact. The Fe content was also found to be 0.045 mmol g^{-1} by ICP analysis performed on the supernatant of an acid-washed sample of the recovered catalyst. The TEM image of the recovered catalyst also revealed a porous polymer without any detectable agglomerated Fe species (Fig. S14). We compared the activity of our catalyst with several previously reported recyclable iron-based systems (Table 3). While most of these catalysts demonstrated good performance, they typically required either relatively large amounts of catalyst or cocatalyst under ambient conditions, or smaller amounts under comparatively harsh conditions. In contrast, our catalyst achieves high activity using only minimal quantities of catalyst and cocatalyst, while operating under mild reaction conditions. This work therefore establishes a proof-of-concept for a sustainable 'dual-role' catalyst design, where an earth-abundant metal ion orchestrates both the assembly of a functional porous matrix and its subsequent application in CO_2 valorization under mild conditions.

Conclusions

In summary, this study highlights the dual functionality of iron catalysts in both the synthesis of covalent triazine frameworks and the cycloaddition of CO_2 to epoxides under mild conditions. The Fe-CTF-3 catalyst, synthesized *via* direct condensation of melamine and dipicolinic acid in the presence of $FeCl_3$, exhibited exceptional surface area and porosity, contributing to its high catalytic efficiency. Systematic investigations into catalyst loading, reaction time, and component roles revealed that Fe centers play a critical role in controlling supersaturation, nucleation, and polymer growth. Control experiments confirmed the synergistic contributions of the CTF structure, nitrogen-rich functionalities, and uniformly dispersed Fe sites to the overall performance. The low Fe content determined by ICP (0.05 mmol g^{-1}) also confirmed that Fe is not a major structural component of CTF but rather acts as a catalytic site for both CTF formation and CO_2 cycloaddition. Notably, Fe-CTF-3 demonstrated excellent activity across a broad range of epoxides and maintained its performance over multiple recycling runs. Given the scarcity of reports on iron-catalyzed CO_2

coupling reactions, these findings offer valuable insights into the design of efficient, low-loading, and sustainable catalysts for carbon capture and utilization. The enhanced CO_2 adsorption capacity, driven by the interplay of physisorption and chemisorption mechanisms, underscores the potential of Fe-CTF-3 as a promising platform for future catalytic applications. This dual-role design principle paves the way for developing a new class of 'self-templating' catalysts, where the metal ion dictates both the support architecture and the catalytic function, particularly for sustainable transformations using abundant metals. While the Fe-CTF-3 framework exhibits excellent recyclability, the need to replenish the TBAB co-catalyst in each cycle poses a limitation from a full-process sustainability perspective. Ongoing work in our group is therefore focused on covalently anchoring Lewis base nucleophiles directly onto the catalyst backbone.

Author contributions

MP: investigation, conducting experiments, data curation, validation. NA: conducting experiments during the revision stage. PM and ST: solid-sate NMR analyses and related discussion. M. K.: conceptualization, funding acquisition, validation, writing-original draft, writing-review & editing, supervision.

Conflicts of interest

There are no conflicts to declare.

Data availability

The data supporting this article have been included as part of the supplementary information (SI). Supplementary information: the procedure for the preparation of homogeneous analogs; BJH pore size distribution and CP-MAS ^{13}C NMR for the Fe-CTF series; CO_2 adsorption capacity for Fe-CTF-3; N_2 adsorption–desorption, BJH pore size distribution, FTIR spectrum, TG pattern, and TEM image for the recovered catalyst; and ^1H NMR spectra for all synthesized compounds. See DOI: https://doi.org/10.1039/d6su00231e.

Acknowledgements

The authors acknowledge IASBS Research Councils for support of this work. This work is based upon research funded by Iran National Science Foundation (INSF) under project No. 4040929.

References

1 J. F. Vollenweider, *Int. Environ. Agreements*, 2013, **13**, 343–367.
2 E. Erdogdu, *WIREs Energy Environ.*, 2025, **14**, e70000.
3 B. B. Rath, S. Krause and B. V. Lotsch, *Adv. Funct. Mater.*, 2024, **34**, 2309060.
4 Y. He, F. H. Müller, R. Palkovits, F. Zeng and C. Mebrahtu, *Appl. Catal., B*, 2024, **345**, 123663.
5 A. J. Kamphuis, F. Picchioni and P. P. Pescarmona, *Green Chem.*, 2019, **21**, 406–448.
6 V. Laserna, G. Fiorani, C. J. Whiteoak, E. Martin, E. C. Escudero-Adán and A. W. Kleij, *Angew. Chem., Int. Ed.*, 2014, **53**, 10416–10419.
7 Q.-W. Song, R. Ma, P. Liu, K. Zhang and L.-N. He, *Green Chem.*, 2023, **25**, 6538–6560.
8 F. Della Monica, A. Buonerba and C. Capacchione, *Adv. Synth. Catal.*, 2019, **361**, 265–282.
9 K. A. Andrea and F. M. Kerton, *Polym. J.*, 2021, **53**, 29–46.
10 E. Fazekas, G. S. Nichol, M. P. Shaver and J. A. Garden, *Dalton Trans.*, 2018, **47**, 13106–13112.
11 A. N. Bilyachenko, V. N. Khrustalev, P. V. Dorovatovskii, L. S. Shul'pina, N. S. Ikonnikov, E. S. Shubina, N. N. Lobanov, V. A. Aliyeva, A. V. M. Nunes, K. T. Mahmudov, Y. N. Kozlov and A. J. L. Pombeiro, *Inorg. Chem.*, 2024, **63**, 1909–1918.
12 J. E. Dengler, M. W. Lehenmeier, S. Klaus, C. E. Anderson, E. Herdtweck and B. Rieger, *Eur. J. Inorg. Chem.*, 2011, 336–343.
13 K. A. Andrea, E. D. Butler, T. R. Brown, T. S. Anderson, D. Jagota, C. Rose, E. M. Lee, S. D. Goulding, J. N. Murphy, F. M. Kerton and C. M. Kozak, *Inorg. Chem.*, 2019, **58**, 11231–11240.
14 M. Adolph, T. A. Zevaco, C. Altesleben, O. Walter and E. Dinjus, *Dalton Trans.*, 2014, **43**, 3285–3296.
15 C. J. Whiteoak, E. Martin, M. M. Belmonte, J. Benet-Buchholz and A. W. Kleij, *Adv. Synth. Catal.*, 2012, **354**, 469–476.
16 M. Taherimehr, J. P. C. C. Serta, A. W. Kleij, C. J. Whiteoak and P. P. Pescarmona, *ChemSusChem*, 2015, **8**, 1034–1042.
17 D. Alhashmialameer, J. Collins, K. Hattenhauer and F. M. Kerton, *Catal. Sci. Technol.*, 2016, **6**, 5364–5373.
18 F. Chen, N. Liu and B. Dai, *ACS Sustainable Chem. Eng.*, 2017, **5**, 9065–9075.
19 Y.-B. Zhou, F. Chen, Z.-H. Du, B.-Y. Liu and N. Liu, *Inorg. Chem.*, 2024, **63**, 16491–16506.
20 E. Y. Seong, J. H. Kim, N. H. Kim, K. H. Ahn and E. J. Kang, *ChemSusChem*, 2019, **12**, 409–415.
21 F. Della Monica, S. V. C. Vummaleti, A. Buonerba, A. De Nisi, M. Monari, S. Milione, A. Grassi, L. Cavallo and C. Capacchione, *Adv. Synth. Catal.*, 2016, **358**, 3231–3243.
22 A. Buonerba, A. De Nisi, A. Grassi, S. Milione, C. Capacchione, S. Vagin and B. Rieger, *Catal. Sci. Technol.*, 2015, **5**, 118–123.
23 M. Fuchs, T. Zevaco, E. Ember, O. Walter, I. Held, E. Dinjus and M. Döring, *Dalton Trans.*, 2013, **42**, 5322–5329.
24 S. Pappuru, D. Shpasser, R. Carmieli, P. Shekhter, F. C. Jentoft and O. M. Gazit, *ACS Omega*, 2022, **7**, 24656–24661.
25 M. Li, J. Zhang, Z. Wei, Y. Gao, Y. Zhao, Y. Teng, H. Wang, R. Zhang and Y. Yang, *ACS Appl. Mater. Interfaces*, 2025, **17**, 20461–20470.
26 S.-N. Zhang, Y.-M. Lin, Q.-J. Wang, J. Yang, Z. Yang, X. Chen, J. Wang and J.-D. Xiao, *ACS Appl. Nano Mater.*, 2025, **8**, 1596–1604.

27 J. Ye, T. Chen, N. Chai, Q. Jiang, Q. Guo, F.-Y. Yi and X. Ma, *Cryst. Growth Des.*, 2025, **25**, 2903–2912.
28 T. Nasiriani, N. A. Nigjeh, S. Torabi and A. Shaabani, *Carbohydr. Polym.*, 2024, **342**, 122418.
29 H.-Q. Yin, M.-Y. Cui, H. Wang, Y.-Z. Peng, J. Chen, T.-B. Lu and Z.-M. Zhang, *Inorg. Chem.*, 2023, **62**, 13722–13730.
30 K. Cho, S. M. Lee, H. J. Kim, Y.-J. Ko, E. J. Kang and S. U. Son, *Chem. –Eur. J.*, 2020, **26**, 788–794.
31 R. Das, S. Kamra and C. M. Nagaraja, *Inorg. Chem. Front.*, 2023, **10**, 2088–2099.
32 Y. Ren, S. Yang and Y. Xu, *Acc. Chem. Res.*, 2025, **58**, 474–487.
33 M. Liu, L. Guo, S. Jin and B. Tan, *J. Mater. Chem. A*, 2019, **7**, 5153–5172.
34 R. Luo, M. Chen, X. Liu, W. Xu, J. Li, B. Liu and Y. Fang, *J. Mater. Chem. A*, 2020, **8**, 18408–18424.
35 R. Luo, M. Chen, F. Zhou, J. Zhan, Q. Deng, Y. Yu, Y. Zhang, W. Xu and Y. Fang, *J. Mater. Chem. A*, 2021, **9**, 25731–25749.
36 A. Iemhoff, M. Vennewald and R. Palkovits, *Angew. Chem., Int. Ed.*, 2023, **62**, e202212015.
37 P. Kuhn, M. Antonietti and A. Thomas, *Angew. Chem., Int. Ed.*, 2008, **47**, 3450–3453.
38 D. Yadav, Subodh and S. K. Awasthi, *Mater. Chem. Front.*, 2022, **6**, 1574–1605.
39 L. Liao, M. Li, Y. Yin, J. Chen, O. Zhong, R. Du, S. Liu, Y. He, W. Fu and F. Zeng, *ACS Omega*, 2023, **8**, 4527–4542.
40 K. Wang, L.-M. Yang, X. Wang, L. Guo, G. Cheng, C. Zhang, S. Jin, B. Tan and A. I. Cooper, *Angew. Chem., Int. Ed.*, 2017, **56**, 14149–14153.
41 H. Zhong, Y. Q. Su, X. W. Chen, X. J. Li and R. H. Wang, *ChemSusChem*, 2017, **10**, 4855–4863.
42 S. Ren, R. Dawson, A. Laybourn, J. Jiang, Y. Khimyak, D. J. Adams and A. I. Cooper, *Polym. Chem.*, 2012, **3**, 928–934.
43 E. Troschke, S. Grätz, T. Lubken and L. Borchardt, *Angew. Chem., Int. Ed.*, 2017, **56**, 6859–6863.
44 Z. Xiang, D. Cao, L. Huang, J. Shui, M. Wang and L. Dai, *Adv. Mater.*, 2014, **26**, 3315–3320.
45 C. B. Meier, R. S. Sprick, A. Monti, P. Guiglion, J.-S. M. Lee, M. A. Zwijnenburg and A. I. Cooper, *Polymer*, 2017, **126**, 283–290.
46 P. Das, G. Chakraborty, N. Friese, J. Roeser, C. Prinz, F. Emmerling, J. Schmidt and A. Thomas, *J. Am. Chem. Soc.*, 2024, **146**, 17131–17139.
47 T. Nouri and M. Khorasani, *J. Phys. Chem. C*, 2024, **128**, 166–176.
48 K. S. Hoseini, M. Razaghi, T. Nouri and M. Khorasani, *Sci. Rep.*, 2023, **13**, 5521.
49 M. Thommes, K. Kaneko, A. V. Neimark, J. P. Olivier, F. Rodriguez-Reinoso, J. Rouquerol and K. S. W. Sing, *Pure Appl. Chem.*, 2015, **87**, 1051–1069.
50 Y.-C. Yuan, B. Sun, A.-M. Cao, D. Wang and L.-J. Wan, *Chem. Commun.*, 2018, **54**, 5976–5979.
51 Y.-F. Chen, Y. Fang, N.-N. Zhu, X. Luo, G.-Y. Zhu, M. Yang, R.-H. Chen, X. Zeng, J.-M. Xiao, L. Liu, G.-H. Ning, D.-S. Bin and D. Li, *Angew. Chem., Int. Ed.*, 2025, **64**, e202424641.
52 V. Campisciano, C. Calabrese, F. Giacalone, C. Aprile, P. L. Meo and M. Gruttadauria, *J. CO2 Util.*, 2020, **38**, 132–140.
53 M. Rashvand and M. Khorasani, *J. CO2 Util.*, 2025, **102**, 103279.
54 P. P. Pescarmona and M. Taherimehr, *Catal. Sci. Technol.*, 2012, **2**, 2169–2187.
55 X. Fang, C. Liu, L. Yang, T. Yu, D. Zha, W. Zhao and W.-Q. Deng, *J. CO2 Util.*, 2021, **54**, 101778.
56 B. Taormina, F. Cecchet, M. Gruttadauria, C. Aprile and F. Giacalone, *J. Environ. Chem. Eng.*, 2026, **14**, 121516.